Massachusetts Institute of Technology

Computational fluid dynamics modeling for performance assessment of permeate gap membrane distillation

Pelin Yazgan-Birgi[1,2], Mohamed I. Hassan Ali[1,3], Jaichander Swaminathan[4],

John H. Lienhard V[4], Hassan A. Arafat[1,2*]

[1] Center for Membrane and Advanced Water Technology, Khalifa University of Science and Technology, Abu Dhabi, United Arab Emirates

[2] Department of Chemical Engineering, Masdar Institute, Khalifa University of Science and Technology, Abu Dhabi, United Arab Emirates

[3] Department of Mechanical Engineering, Masdar Institute, Khalifa University of Science and Technology, Abu Dhabi, United Arab Emirates

[4] Rohsenow Kendall Heat Transfer Laboratory, Department of Mechanical Engineering, Massachusetts Institute of Technology, Cambridge MA 02139-4307, USA

* Corresponding author. P.O. Box 54224, Abu Dhabi, United Arab Emirates, hassan.arafat@ku.ac.ae

Abstract

The critical factors and interactions which affect the module-level performance of permeate gap membrane distillation (PGMD) were investigated. A three-dimensional computational fluid dynamics (CFD) model was developed for the PGMD configuration, and the model was validated using experimental data. The realizable k-ε turbulence model was applied for the flow in the feed and coolant channels. A two-level full factorial design tool was utilized to plan additional simulation trials to examine the effects of four selected parameters (i.e., factors) on permeate flux and thermal efficiency, both of which represent performance indicators of PGMD. Permeate gap conductivity (k_{gap}), permeate gap thickness (δ_{gap}), module length (L_{module}), and membrane distillation coefficient (B_m) were the selected factors for the analysis. The effect of each factor and their interactions were evaluated. B_m was found to be the most influential factor for both performance indicators, followed by k_{gap} and δ_{gap}. The factorial analysis indicated that the influence of each variable depends on its interactions with other factors. The effect of k_{gap} was more significant for membranes with higher B_m because the gap resistance becomes dominant at high B_m. Similarly, δ_{gap} is inversely proportional to the permeate flux and only significant for membranes with high B_m.

Nomenclature

38

39

A	Active area [m^2]
B_m	Membrane distillation coefficient [kg/m^2 Pa s]
c_p	Heat capacity [kJ/kg K]
$\dot{F}$	Volumetric flow rate [L/min]
g	Gravitational constant [m/s^2]
h_f	Heat transfer coefficient along the feed side boundary layer [W/m^2 K]
h_{fg}	Latent heat of evaporation [kJ/kg]
h_p	Heat transfer coefficient in the permeate gap [W/m^2 K]
J	Permeate mass flux [kg/m^2 s]
k	Turbulent kinetic energy
k_{gap}	Permeate gap thermal conductivity [W/m K]
k_{gas}	Thermal conductivity of the gas trapped in the membrane pores [W/m K]
k_m	Membrane thermal conductivity [W/m K]
k_{solid}	Solid membrane material thermal conductivity [W/m K]
L_{module}	Module length [m]
$\dot{m}$	Mass flow rate [kg/s]
P	Pressure [Pa]
P^{vap}	Partial vapor pressure [Pa]
S_h	Energy source term [J/m^3]
S_j	Mass source term [kg/m^3]
S_m	Momentum source term [kg m/s m^3]
T_f	Feed stream temperature [K]
T_p	Permeate gap stream temperature [K]
$\dot{q}$	Heat flux [W/m^2]
$\dot{Q}_{in}$	Total heat input [W]
u	Fluid velocity [m/s]
W	Module width [mm]

40

Greek symbols

41

δ	Thickness [m]
ε	Porosity [-]
μ	Viscosity [Pa s]

42

Subscripts and superscripts

43

ave	Average
BL	Boundary layer
c	Cooling channel

c, p	Cooling plate/permeate gap interface
cond	Conduction
f	Feed channel
gap	Permeate gap
in	Inlet
m	Membrane
m,f	Membrane/feed interface
m,p	Membrane/permeate gap interface
out	Outlet
p	Permeate stream
plate	Cooling plate
vap	Water vapor

44

1. Introduction

Membrane distillation (MD) has the potential to become an important brine concentration technology [1,2]. In addition to the four common MD configurations (direct contact MD or DCMD; vacuum MD or VMD; sweeping gap MD or SGMD; and air gap MD or AGMD), permeate gap MD (PGMD) has developed more recently [3–7]. PGMD, which is also called water gap MD or liquid gap MD in literature, is a hybrid of the DCMD and AGMD configurations [8–11]. An additional channel (the permeate gap) separates the permeate stream from the cooling stream with an impermeable condensing plate. Other versions of PGMD have been studied, including material gap MD (e.g., with sand in the gap) and conductive gap MD (with a thermally-conductive material in the gap, which provides high energy efficiency and permeate flux [4]).

Since conductive heat loss is challenging to minimize in DCMD, DCMD has lower thermal efficiency than AGMD [12]. On the other hand, the presence of an air gap in AGMD adds an extra mass transfer resistance to vapor transport. Therefore, AGMD has lower permeate flux than DCMD. Separating the permeate stream from the cooling liquid enables the utilization of any liquid (such as the incoming feed itself) as a coolant medium in PGMD, in contrast to DCMD which requires a pure cold water stream [13]. Moreover, the mass transfer mechanism is improved in PGMD, resulting in higher permeate flux than AGMD [4]. Cipollina et al. reported that PGMD showed markedly better performance than AGMD even under mild process conditions with the smaller temperature difference between the feed and permeate streams [14]. Winter [15] studied pilot-scale AGMD, PGMD, and DCMD modules to compare the energy efficiency (which was quantified with gained output ratio or *GOR*) and the productivity (permeate flux) of these systems. It was found that the *GOR* and permeate flux values of PGMD and DCMD were within the same range. On the other hand, AGMD exhibited a markedly lower performance (in terms of lower *GOR* and permeate flux values) than the PGMD and DCMD configurations.

In small-scale (i.e., experimental) modules, the energy efficiency of MD is quantified by the ratio between the heat transferred due to vapor flux ($\dot{Q}_{vap}$) and the total heat transferred through the membrane ($\dot{Q}_{total}$) [2,7]. This ratio is called the thermal efficiency, and GOR is proportional to it [7]. The total heat transferred includes $\dot{Q}_{vap}$ and heat transferred across the membrane thickness via conduction ($\dot{Q}_{cond}$). If an MD module has high thermal efficiency (≈ 1), the membrane in that module likely has a relatively low mass transfer resistance and/or a high conductive heat transfer

5

75 resistance under the process operating conditions [16]. Thermal efficiency not only depends on the

76 operating parameters but also on structural parameters such as membrane properties and module

77 geometry [17].

78 Since the permeate gap is responsible for most of the heat transfer resistance in PGMD, gap

79 properties, such as gap conductivity (k_{gap}) and gap thickness (δ_{gap}), are considered important

80 factors affecting the PGMD efficiency [6]. The membrane itself is also a dominant resistance

81 within the MD module. The membrane properties, such as its MD coefficient (B_m), are believed to

82 have a lower impact on the PGMD performance than that of AGMD [6]. Swaminathan et al.

83 investigated PGMD performance using a numerical model based on counter-flow heat exchanger

84 theory (number of transfer units method) [6]. The effect of δ_{gap} was found inversely proportional

85 to the *GOR* [6], which was supported by the experimental data from [15]. Similarly, Eykens et al.

86 reported a flux decline while increasing δ_{gap} from 0 to 2 mm [8]. In contrast, the opposite trend

87 was reported by [10], where significant flux enhancement was observed when increasing δ_{gap} from

88 9 to 13 mm. In another study, a one-dimensional numerical model was developed to explore the

89 critical parameters for the energy efficiency of PGMD and conductive gap MD [4]. The study

90 reported that increasing δ_{gap} and k_{gap} have both enhanced the *GOR*, although increasing k_{gap} above

91 10 W/m K did not have a significant effect [4]. Cheng et al. reported that a PGMD setup with a

92 brass net, which had a k_{gap} over 100 W/m·K (instead of polypropylene net with $k_{gap} = 0.17$ W/m·K),

93 did not improve the PGMD performance markedly [5]. In large-scale PGMD and DCMD modules,

94 the modules with longer feed channels have better energy efficiency but permeate flux decline is

95 observed as well [18,19].

96 Process operating parameters also influence the MD process performance. Ruiz-Aguirre et al.

97 applied the factorial design tool for a pilot-scale spiral wound PGMD configuration to assess the

98 effects of feed and coolant inlet temperatures, feed flow rate and their interactions on the PGMD

99 process performance experimentally [20]. They concluded that feed inlet temperature has a

100 substantial influence on both permeate flux and specific thermal energy consumption.

101 Furthermore, the interaction between the feed inlet temperature and feed flow rate was found to

102 be significant for permeate flux. Recently, a modeling study on PGMD module performance was

103 published, which studied the effects of feed flow rate and temperature on process performance

104 [21]. However, although the effects of operating parameters on PGMD performance were

105   discussed in [21] and others in the literature, no modeling studies have reported on the effects of

106   interactions between module and membrane properties (includes effects of k_{gap}, δ_{gap}, B_m, module

107   length (L_{module}) and their interactions) on PGMD performance.

108   Computational fluid dynamics (CFD) was demonstrated as a useful tool to investigate the

109   parameters influencing the MD process performance [22,23]. Several two-dimensional and three-

110   dimensional CFD studies were employed to design improved MD processes and propose solutions

111   to issues in existing configurations [23]. Thus, in the present study, a three-dimensional CFD

112   model was first developed for a laboratory-scale PGMD configuration and was validated using

113   experimental PGMD data. Then, additional simulation runs were designed using a two-level full

114   factorial design tool. The factorial design tool was utilized as it helps account for all likely high

115   and low combinations of the selected factors in the runs and provides information about the effects

116   of factors and their interactions on the output [24,25]. The parameters k_{gap}, δ_{gap}, B_m, and L_{module}

117   were the selected factors in our study. Permeate flux and thermal efficiency, which are critical MD

118   performance indicators, were obtained from the CFD simulations. Finally, the effects of the four

119   factors and their interactions were evaluated based on the obtained results.

120

2.   Theory

2.1   Heat and mass transfer in PGMD

123   In the PGMD configuration (Fig. 1), a hydrophobic membrane is in direct contact with the feed

124   and permeate sides. It is assumed that the permeate gap is entirely filled with permeate liquid with

125   permeate overflow leaving the channel from the top. The permeate gap and coolant plate introduce

126   additional heat transfer resistances in the system (compared to DCMD), which have to be

127   considered in the PGMD model. The vapor flow through the membrane pores is induced by the

128   partial pressure difference between the feed and permeate sides. The total transmembrane mass

129   flux (J, kg/m^2 s) can be defined as follows:

$$J = B_m \cdot \left(P_{m,f}^{vap} - P_{m,p}^{vap} \right) = B_m \, \Delta P^{vap} \tag{1}$$

130   where B_m is the membrane distillation coefficient (kg/m^2 Pa s), $P_{m,f}^{vap}$ is the vapor pressure on the

131   membrane/feed interface (Pa), $P_{m,p}^{vap}$ is the vapor pressure on the membrane/permeate gap interface

132 (Pa) and ΔP^{vap} is the partial pressure difference between the feed and permeate gap sides. $P_{m,f}^{vap}$

133 and $P_{m,p}^{vap}$ depend on the temperatures at the membrane surface on the feed ($T_{m,f}$) and permeate

134 gap ($T_{m,p}$) sides, respectively.

135
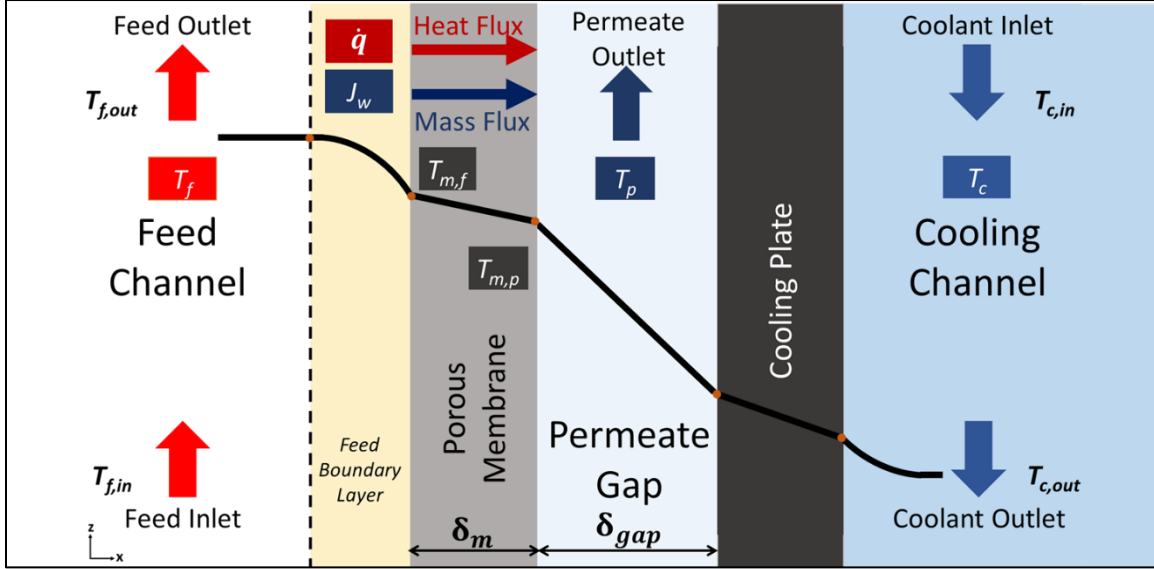
136

137 **Fig. 1.** Schematic representation of PGMD configuration in the counter-current flow mode. The
138 configuration includes the feed channel with the feed boundary layer, the porous hydrophobic
139 membrane, the permeate gap channel, the cooling plate, and the cooling channel. T_f, T_p and T_c
140 represent the local bulk stream temperatures along the feed, permeate gap and cooling channels,
141 respectively. These temperatures vary along the channels due to the heat transfer along the module.

142

143 The vapor pressure of water (P^{vap}) can be calculated by the Antoine equation [26]:

$$P^{vap} = exp\left(23.1964 - \frac{3816.44}{T - 46.13}\right) \tag{2}$$

144 where T is the temperature (K). Since pure water was used as the feed stream in our experiments,
145 vapor pressure depression was not considered in our model.

146 Mass and heat transfer occur simultaneously. The heat flux is a function of vapor flux, J. The
147 overall J can be calculated by integrating the local flux, $J(y,z)$, over the full membrane surface as
148 follows:

$$J = \frac{1}{A} \iint J(y,z)\, dy\, dz \tag{3}$$

$$J = \frac{B_m}{A} \iint \Delta P^{vap}(y,z)\, dy\, dz \tag{3a}$$

$$J = \frac{B_m}{A} \left[\iint P_{m,f}^{vap}(y,z)\, dy\, dz - \iint P_{m,p}^{vap}(y,z)\, dy\, dz \right] \tag{3b}$$

149   where A is the active membrane area (m^2) and the (y, z) coordinate represents the location on the

150   membrane surface at the feed/membrane or permeate gap/membrane interface.

151   The heat flux $(\dot{q})$ across the system components in the x-direction (Fig. 1) is the same under steady-

152   state conditions

$$\dot{q} = \dot{q}_{BL,f} = \dot{q}_m = \dot{q}_p = \dot{q}_c \tag{4}$$

$$\dot{q}_{BL,f} = h_f \left(T_f - T_{m,f} \right) \tag{5}$$

153   where $\dot{q}_{BL,f}$, $\dot{q}_m$, $\dot{q}_p$, and $\dot{q}_c$ are the heat fluxes through the feed side boundary layer, the membrane,

154   the permeate gap and the cooling system, respectively. h_f is the heat transfer coefficient for the

155   feed side boundary layer (W/m^2 K). In this study, the heat transfer in the feed channel is evaluated

156   using the 3D CFD model. Based on this model, the heat transfer coefficient across the feed side

157   boundary layer can be inferred.

158   ***Membrane side***

159   The overall heat flux through the membrane, $\dot{q}_m$, can be expressed as follows:

$$\dot{q}_m = \dot{q}_{vap} + \dot{q}_{cond} \tag{6}$$

160   where $\dot{q}_{cond}$ and $\dot{q}_{vap}$ are the conductive heat flux and the heat flux due to evaporation at the pore

161   entrance, respectively. Since the mass and heat transfer phenomena happen simultaneously, the

162   heat flux through the membrane thickness is a function of permeate flux, J, through the membrane.

163   Thus, $\dot{q}_{vap}$ can be expressed as

$$\dot{q}_{vap} = J\, h_{fg} \tag{7}$$

164   where h_{fg} is the latent heat of evaporation. Heat flux across the membrane thickness due to

165   conduction can be calculated from

$$\dot{q}_{cond} = \frac{k_m}{\delta_m}\left(T_{m,f} - T_{m,p}\right) = h_{m,cond}\,\Delta T \tag{8}$$

166   where ΔT is the temperature difference between the opposing membrane sides, $h_{m,cond}$ is the

167   membrane conductive heat transfer coefficient (W/m^2 K) and k_m is the thermal conductivity of

168   the membrane (W/m K), which is calculated from the simple approximation:

$$k_m = \varepsilon\, k_{gas} + (1 - \varepsilon)\, k_{solid} \tag{9}$$

169   where k_{gas} is the thermal conductivity of the gas (air and vapor) trapped within the membrane

170   pores (W/m K), k_{solid} is the thermal conductivity of the solid membrane material (W/m K), and ε

171   is the porosity of the membrane. The gas thermal conductivity is usually far lower than the solid

172   membrane conductivity, so in order to minimize the conductive heat losses k_m must be as low as

173   possible or ε high as high as possible. By substitution in Eqn. 6, $\dot{q}_m$ becomes:

$$\dot{q}_m = J\, h_{fg} + h_{m,cond}.\Delta T \tag{10}$$

174

Permeate gap channel

176   In the permeate gap channel, permeate liquid fills the gap completely and the permeate overflow

177   leaves the channel from the top. Since the liquid in the channel is almost stagnant, heat transfer

178   through the permeate channel is by conduction only and there is no boundary layer on the

179   permeate-gap side of the membrane. The heat flux through the permeate gap, $\dot{q}_p$, can be expressed

180   as:

$$\dot{q}_p = h_p\left(T_{m,p} - T_{c,p}\right) \tag{11}$$

181   where h_p is the heat transfer coefficient through the whole thickness of the permeate gap (W/m²

182   K) and $T_{c,p}$ is the temperature at the permeate gap/cooling plate interface. h_p can also be expressed

183   as

$$h_p = \frac{k_{gap}}{\delta_{gap}} \tag{12}$$

184   where k_{gap} and δ_{gap} are the thermal conductivity and thickness of the permeate gap, respectively.

185   If there is no spacer in the permeate gap channel, then $\dot{q}_p$ is only determined by the thermal

186   conductivity of the fresh water (k_{water}) in the gap ($k_{gap} = k_{water}$). Increasing k_{gap} leads to better

187   process performance, the opposite effect of increasing k_m [7].

188   ***Cooling system***

189   Heat is transferred from the permeate gap to the coolant liquid via a combination of thermal

190   resistances including those of cooling plate and the cooling channel.

$$\dot{q}_c = h_{c,total} \left(T_{c,p} - T_c \right) \tag{13}$$

$$\frac{1}{h_{c,total}} = \frac{1}{h_{plate}} + \frac{1}{h_c} \tag{14}$$

191

192   where $h_{c,\,total}$, h_{plate} and h_c represent the heat transfer coefficients through the cooling system, the

193   heat transfer coefficient through the cooling plate ($h_{plate} = k_{plate}/\delta_{plate}$), and the heat transfer

194   coefficient through the cooling channel, respectively.

195   Thermal efficiency (η) is the fraction of energy transferred from the hot feed stream to the cold

196   permeate side that is actually utilized in mass transfer [17]. η is calculated from

$$\eta = \frac{\dot{Q}_{vap}}{\dot{Q}_{vap} + \dot{Q}_{cond}} \tag{15}$$

197   where $\dot{Q}_{vap}$ is the rate of heat transfer from the feed to the permeate due to the mass transfer (W)

198   and $\dot{Q}_{cond}$ is the rate of heat transfer due to conduction through the membrane ($\dot{Q}_{cond} = \dot{q}_{cond}\, A$).

11

199   When η is close to unity, most of the heat delivered to the MD module is consumed via the

200   evaporation process and conductive heat losses are negligible. Membrane properties and MD

201   operational parameters have a significant influence on η [17].

202

2.2   Governing transport equations in the CFD model

204   Since k-ε models have been validated and found reliable for various MD configurations (AGMD,

205   DCMD and VMD) [27–32], the realizable two-layer k-ε model was applied to model the turbulent

206   flow in the feed and permeate channels. A turbulent eddy-viscosity was considered as a function

207   of the turbulent kinetic energy (k) and turbulent dissipation rate (ε) terms in the model [33]. This

208   model is one of the Reynolds-Averaged Navier-Stokes equations which approximate the

209   representation of the physical phenomena of turbulence. The transport equations govern the

210   transport of the mean flow quantities. In order to model the stress tensor, the Reynolds stress

211   transport models and Boussinesq approximation (which is an eddy viscosity model) were

212   employed. Further details can be found in [34,35].

213   The contributions of J and $\dot{q}_{vap}$ were included in the three Reynolds-averaged conservation

214   equations: conservation of mass (16), conservation of momentum (17) and conservation of energy

215   (18).

$$\nabla.(\rho\vec{v}) = S_j \tag{16}$$

$$\nabla.(\rho\vec{v}\vec{v}) = -\nabla P + \nabla.(\vec{\tau}) + \rho\vec{g} + S_m \tag{17}$$

$$\nabla.(\rho c_p T\vec{v}) = \nabla.(k\nabla T) + S_h \tag{18}$$

216   where S_j, S_m, and S_h are mass, momentum and energy source terms, respectively, and can be

217   calculated from [36]

$$S_j = \begin{cases} -\dfrac{J\,A}{V} & \text{at the feed/membrane interface} \\[2mm] \dfrac{J\,A}{V} & \text{at the permeate gap/membrane interface} \end{cases} \tag{16a}$$

12

$$
S_m = \begin{cases} -\dfrac{J\,A\,u}{V} & \text{at the feed/membrane interface} \\[2mm] \dfrac{J\,A\,u}{V} & \text{at the permeate gap/membrane interface} \end{cases}
\tag{17a}
$$

$$
S_h = \begin{cases} -\dfrac{\dot{q}_{vap}A}{V} & \text{at the feed/membrane interface} \\[2mm] \dfrac{\dot{q}_{vap}A}{V} & \text{at the permeate gap/membrane interface} \end{cases}
\tag{18a}
$$

218   where u is the feed velocity (m/s) in the flow direction and V is the fluid element volume (m³).

219

3.   Methodology

3.1.   PGMD experimental set-up

222   A laboratory scale PGMD setup was used for the experiments, as illustrated in Fig. 2. The
223   experimental setup has two flow loops for hot feed and coolant streams. Since MD in the counter-
224   current flow mode (in terms of coolant and feed streams) has shown better performance than the
225   co-current mode [4], the experiments were performed in the former mode. The system included a
226   flat sheet hydrophobic PVDF membrane (ISEQ00010 Millipore). The module and membrane
227   properties are listed in Table 1. The membrane active area was 192 cm². An aluminum plate was
228   used as the cooling plate. The feed and permeate channels had inner dimensions of 16 cm × 12
229   cm. A plastic spacer was used in the permeate gap channel to keep the permeate gap thickness
230   constant. Also, an additional woven spacer mesh was placed in between the membrane and plastic
231   spacer to protect the membrane from any damage due to the hard edges of the plastic mesh. In the
232   module, the design of the feed flow channel included a flow developing region before the feed
233   stream entrance to achieve a fully developed feed inlet flow condition when the feed stream
234   reached the active membrane area. Further details of the experimental apparatus are given in [37].

235

236   **Table 1.** PGMD module and membrane properties.

Property	Value
Module length, L_{module}	16 cm
Module width, w	12 cm
Feed flow channel depth	4 mm
Membrane type	PVDF membrane (ISEQ00010 Millipore)
Membrane thickness, δ_m	200 µm
Nominal membrane pore diameter	0.2 µm
Porosity, ε	0.80
MD coefficient, B_m	18 x 10^{-7} kg/m^2 Pa s
Membrane thermal conductivity (k_m) [a]	0.07332 W/m K
Permeate gap thickness, δ_{gap}	1 mm
Cooling plate thickness	4.8 mm
Coolant flow channel depth	10 mm

237   [a] Calculated from Eq. (9) where k_{gas} is equal to the thermal conductivity of the vapor ($k_{vapor} = 0.0261$ W/m K) and
238   k_{solid} is the thermal conductivity of the PVDF ($k_{PVDF} = 0.2622$ W/m K) [38,39].

239

240   **3.2. PGMD Experimental procedure**

241   The PGMD experiments were performed at four feed flow rates, $\dot{F}_f$ (3.87, 7.94, 12.13, and 15.92

242   L/min). Pure water was used as feed solution in our experiments. The conductivity of the feed and

243   permeate water streams were measured to monitor for membrane wetting and purity of the

244   freshwater produced. The average feed conductivity was 298 µS/cm while the average permeate

245   conductivity remained below 11.8 µS/cm during the experiments. This guaranteed that pore

246   wetting was avoided during the experiments. The process operating conditions are summarized in

247   Table 2. First, the feed stream was heated to 63.4 °C at the adjusted pressure and $\dot{F}_f$ condition.

248   Similarly, the cooling water was kept at 21.2 °C with a constant cooling water flow rate ($\dot{F}_c$) of

249   10.99 L/min. The stream temperatures were monitored using pipe plug thermistor probes

250   (designated with temperature sensor symbol (**T**) in Fig. 2a). The $\dot{F}_f$ values yielded a Reynolds

251   number range (2100 ≤ Re ≤ 9100), which includes the transition to turbulent flow regime. Stable

252   values were obtained for the flow rates and temperatures of the streams after 2.5 hours. Then, each

253   experiment was continued for an additional 1.5 hours to obtain a stable permeate flux (J) under

254   steady state condition. Each set of experiments was repeated three times to check repeatability.

255   Finally, the experimental data were compared with the CFD simulation results to validate the

256   developed model, which was also based on the same operating conditions used in the experiments.

257

258
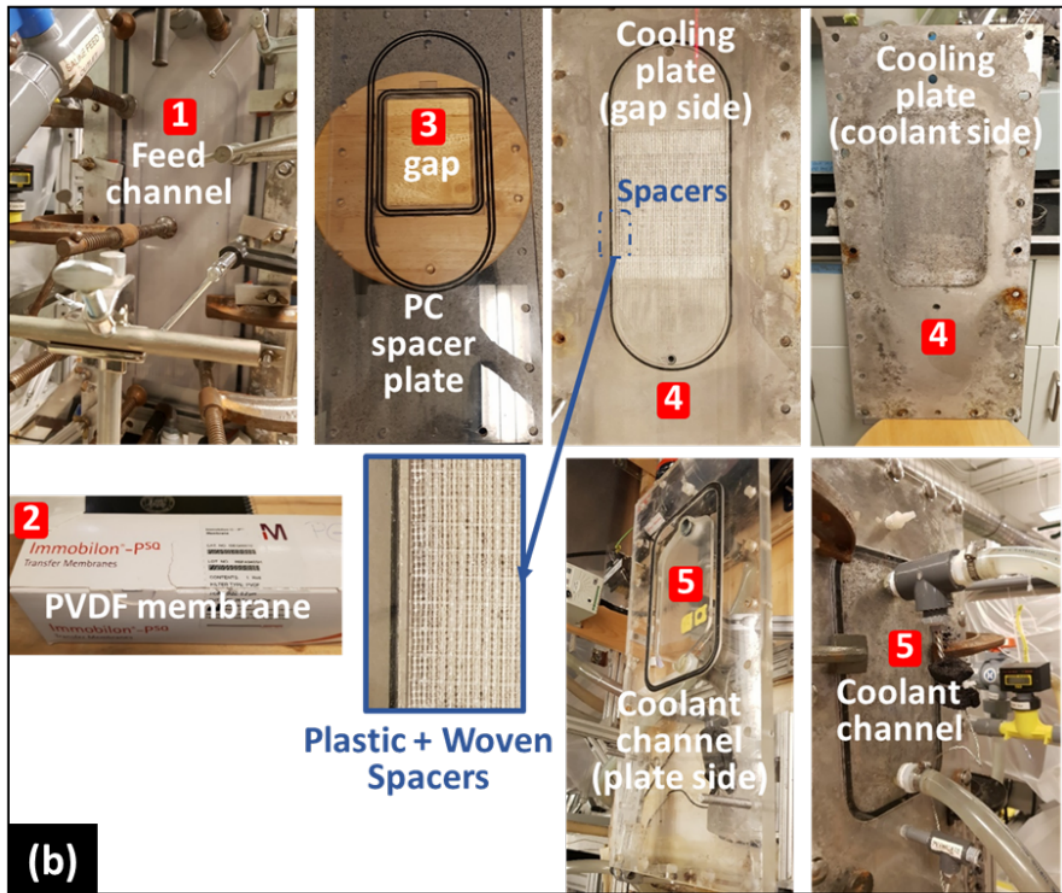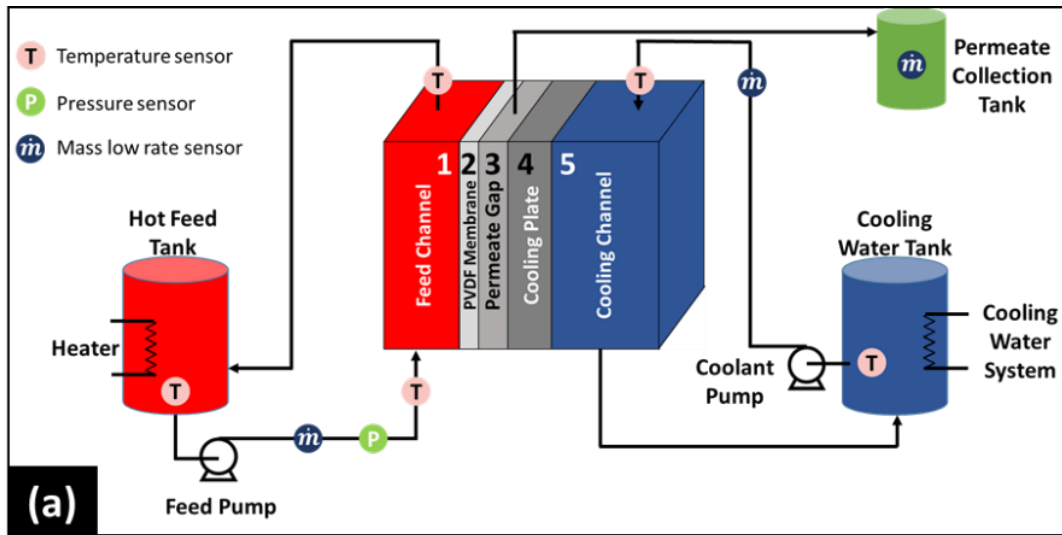
Fig. 2. (a) Schematic representation of the PGMD experimental setup, (b) PGMD system parts: 1-feed channel, 2- PVDF membrane, 3- permeate gap channel, 4- aluminum cooling plate, 5- coolant channel and spacers (plastic and woven) along the permeate gap channel.

262

15

263 **Table 2.** Summary of the operating conditions during the PGMD experiments

| Variable	Value
Feed inlet temperature ($T_{f,\ in}$)	63.4 °C
Feed inlet volumetric flow rate ($\dot{F}_f$)	3.87, 7.94, 12.13, 15.92 L/min
Feed inlet gauge pressure ($P_{f,\ in}$)	0.34 bar
Gap outlet gauge pressure ($P_{gap,\ out}$)	0 bar
Coolant inlet temperature ($T_{c,in}$)	21.2 °C
Coolant inlet volumetric flow rate ($\dot{F}_c$)	10.99 L/min

264

3.3. CFD model setup

266 The CFD model runs were performed using the Star-CCM+ package (double precision Star-
267 CCM+12.06.010-R8, Siemens Product Lifecycle Management Software Inc., Plano, Texas [33]).
268 In the CFD model, a steady-state condition was assumed within the PGMD process. Since the feed
269 and cooling channels flows were within the transition/turbulent flow ranges ($2100 \leq Re \leq 9100$ in
270 our experiments), a realizable two-layer k-ε turbulence model was applied. The feed, permeate
271 gap and coolant streams were set as freshwater. In the experiments, the permeate gap was filled
272 with stagnant permeate liquid. Additionally, a plastic spacer was placed in the channel to support
273 the membrane and keep the permeate gap thickness constant. Since the porosity of the spacer was
274 large (around 80%) and the thermal conductivity of water ($k_{water} \approx 0.60$ W/m K) is much higher
275 than that of the plastic spacer ($k_{spacer} \approx 0.15$ W/m K), the thermal conductivity of the permeate gap
276 was considered to be that of freshwater in the baseline case in our CFD model ($k_{water} \approx 0.60$ W/m
277 K).

Geometry and boundary conditions

279 The experimental conditions explained in the previous section and provided in Table 2, were used
280 as the basis of the CFD model. To develop the model, a three-dimensional geometry was built
281 based on the properties in Table 1. The general scheme of this geometry is presented in Fig. 3a.
282 The inset figure illustrates the module parts and the direction of the applied inlet and outlet
283 conditions on the boundaries. The feed, permeate gap, and cooling channels were set as fluid
284 domains and the membrane and cooling plate were defined as solid volumes. Feed inlet, feed
285 outlet, permeate outlet, coolant inlet, and coolant outlet boundaries were set based on the
286 experimental conditions given in Table 2. The boundaries for the inlets and outlets were set as

16

287   velocity inlets and pressure outlets, respectively. The coolant and permeate outlet boundaries were

288   open to atmospheric pressure. All the sidewall boundaries other than the inlet and outlet boundaries

289   were considered as no-slip walls. The internal interface boundaries (the feed/membrane interface,

290   the membrane/permeate gap interface, the permeate gap/cooling plate interface and the cooling

291   plate/cooling channel interface) were selected as conjugate heat transfer boundaries, which allow

292   conjugate heat transfer between the regions (between a fluid domain and a solid domain) in Star-

293   CCM+. This strategy allows the simulation of heat transfer between a solid domain and a fluid

294   domain by exchanging thermal energy at the boundary between the two domains, so that heat

295   transport can be solved for at the wall correctly. In order to include the energy sink and source

296   terms, the heat flux was specified at the relevant interfaces such as the feed/membrane interface

297   (where energy leaves the feed volume), and the membrane/permeate gap interface (where energy

298   enters the permeate gap volume). Then, these terms were linked with an expression defined for

299   calculating $\dot{q}_{vap}$. The mass and momentum source terms were similarly set and linked with an

300   expression defined for calculating J. J was monitored over a range of inlet feed volumetric flow

301   rates ($\dot{F}_f$): 3.87, 7.94, 12.13, and 15.92 L/min. In the CFD model, the thermal conductivity of the

302   permeate gap (k_{gap} = 0.6 W/m K) and membrane distillation coefficient (B_m = 18 x 10^{-7} kg/m^2 s

303   Pa) were selected based on the reported data for a similar setup and the same type of membrane
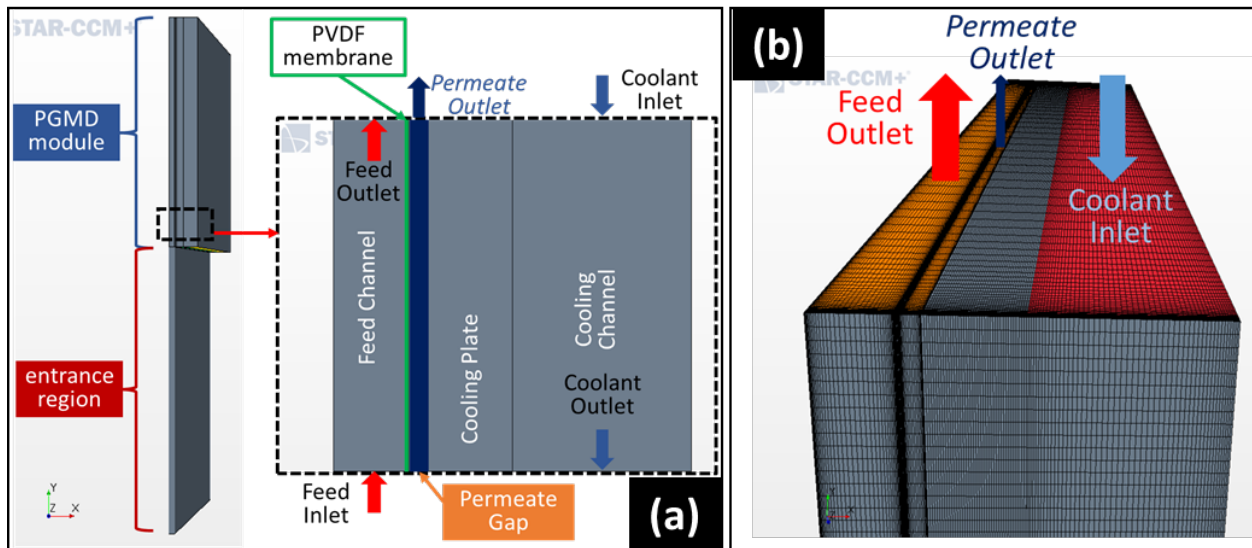
304   [6].

Fig. 3. (a) CAD drawing of the PGMD domain and its subdomain representation (Feed stream entrance region and MD module subdomains including the feed, permeate gap and cooling

17

308 channels, and the PVDF membrane and cooling plate solid domains with the boundaries), (b) the
309 structure of the mesh from the top view of the PGMD module.

310

Mesh operation

312 The directed mesh operation was applied to generate a 3D solver mesh in Star-CCM+ [33]. A mesh

313 independence analysis was performed to achieve reliable results from the simulations. Permeate

314 flux was chosen as a comparison parameter to ensure that flux results are grid-size-independent.

315 The mesh size was refined step by step with considering all three dimensions and the permeate

316 flux results were compared. When the change in permeate flux was less than 1%, the mesh

317 refinement stopped. For the validation model, 240 number of divisions along the module length

318 and 120 number of divisions along the module width were created as a base for the directed mesh

319 operation. Then, the operation was continued for the feed channel, membrane, permeate gap, and

320 cooling channel thicknesses, which were divided into 40, 20 and 50 layers, respectively. A two-

321 sided hyperbolic stretching factor was applied for the domains (spacing at the wall boundaries was

322 started at 0.01 mm.). The stretching factor was used to achieve further mesh refinement near the

323 wall boundaries and to monitor the boundary layers of the feed and cooling water streams. The

324 cooling plate and membrane were divided into 40 and 10 layers, respectively. Additionally, a

325 volume extruder was applied to create 20 cm entrance length before the feed inlet boundary. This

326 entrance region was included in the model to achieve a fully developed feed inlet condition when

327 the feed stream reaches the active membrane area. Heat losses were neglected at the entrance

328 region. In total, $1,305 \times 10^4$ elements were generated for the domain. The structure of the mesh

329 from the top view of the PGMD module is shown in Fig. 3b.

Software tool

331 A finite volume numerical discretization scheme based Star-CCM+ commercial software was used

332 to solve the model equations described above. Pre-processing step was also performed utilizing

333 the CAD and meshing packages provided in the Star-CCM+ software. SIMPLE algorithm was

334 implemented to control the overall solution. Segregated flow and segregated energy solvers were

335 set and the second-order upwind numerical scheme was used for the numerical solution. Under-

336 relaxation factors (URFs) were defined for solvers such as velocity solver (URF= 0.7), pressure

337 solver (URF= 0.3), fluid energy (URF= 0.8), and solid energy (URF= 0.9). The URF value governs

18

338 the new level to which the newly computed data from the solution replaces the old data for each

339 iteration step [33]. J and $\dot{q}_{vap}$ were calculated and fed into the solution of the governing CFD

340 model equations (Eqs. 16– 18) through the source terms (Eqs. 16a–18a) for each iteration step. It

341 continued until the solver converged to represent the local hydrodynamic and thermal properties

342 within the solution domain. The convergence criteria were achieved when the flow rate of fluid

343 entering and leaving the model balanced and the temperature and J plots became stable. The

344 residuals of the continuity and momentum equations were maintained below 10^{-12}, and the residual

345 of the energy equation was maintained below 10^{-5}. It took an average 45,000 iterations to reach

346 the residual levels.

347

348 **3.4. Design of the simulation runs: Two-level full factorial design**

349 Factorial analysis is a useful statistical approach, which can be applied in the design of both

350 experiments and modeling studies [40]. The technique is used to study the impact of multiple

351 independent variables, each of which may assume different possible values (i.e., levels), on one or

352 more dependent variables. All potential high and low combinations of the input factors were

353 considered in a two-level full factorial design to plan the runs for an experimental or modeling

354 study [24,25,40]. Design-Expert ® Version 10 (Stat-Ease Inc., Minneapolis [41]) was used to

355 design the simulation runs. The relative effects of four selected key factors and their interactions

356 were elucidated in this study: k_{gap}, δ_{gap}, L_{module} and B_m. A CFD simulation was performed for each

357 run under the process operating conditions provided earlier (Table 2).

358 The following inputs were used in all simulation runs; $T_{f,\,in}$ = 63.4 °C, $\dot{F}_f$ =3.87 L/min, $P_{gap,out}$ = 0

359 bar (gauge pressure), $T_{c,in}$ = 21.2 °C, and $\dot{F}_c$ = 10.99 L/min. The module and membrane properties

360 were the same as in Table 1, but the selected four variables (k_{gap}, δ_{gap}, L_{module}, and B_m) were varied

361 for each run. The design matrix of the runs at two levels of input parameters (lower– and upper–

362 bounded intervals) are presented in Table 3. The positive (+) and negative (–) signs for each factor

363 indicate two-levels which are the lower and upper bounds, respectively. The total number of factor

364 combinations is based on the 2^n rule [25], where n is the number of factors (4 in this case).

365 The levels (lower and upper bounds) were selected based on a thorough review of the reported

366 values for each factor found in the literature. For instance, since increasing k_{gap} or B_m does not

367 have a significant influence on the permeate flux beyond a specific limit [4,6], the upper bounds

368 of the k_{gap} and B_m were set at 10 W/m K and 20 x 10^{-7} kg/m^2 s Pa, respectively. The lower bound

369 of the k_{gap} was kept equal to the thermal conductivity of water, which is 0.6 W/m K. The responses

370 (J and η) from each CFD run were fed into the Design-Expert software to analyze the effects of

371 factors statistically. A 95% confidence level was used in the analysis.

372

373 **Table 3.** Design matrix table for the CFD simulation runs based on a two-level full factorial design
374 (four main factors: gap conductivity (k_{gap}), gap thickness (δ_{gap}), MD coefficient (B_m) and module
375 length (L_{module})). A total of 16 CFD runs were performed.

| Run	k_{gap}	δ_{gap}	B_m	L_{module}	k_{gap} [W/m K]	δ_{gap} [mm]	B_m [kg/m^2 s Pa]	L_{module} [cm]
1	+	+	+	+	10	3	2 x 10^{-6}	32
2	-	-	+	-	0.6	0.5	2 x 10^{-6}	16
3	+	-	+	+	10	0.5	2 x 10^{-6}	32
4	-	-	-	-	0.6	0.5	1 x 10^{-7}	16
5	+	-	-	-	10	0.5	1 x 10^{-7}	16
6	-	+	-	-	0.6	3	1 x 10^{-7}	16
7	+	-	+	-	10	0.5	2 x 10^{-6}	16
8	-	+	-	+	0.6	3	1 x 10^{-7}	32
9	+	+	-	+	10	3	1 x 10^{-7}	32
10	-	-	-	+	0.6	0.5	1 x 10^{-7}	32
11	-	+	+	-	0.6	3	2 x 10^{-6}	16
12	-	+	+	+	0.6	3	2 x 10^{-6}	32
13	+	-	-	+	10	0.5	1 x 10^{-7}	32
14	+	+	+	-	10	3	2 x 10^{-6}	16
15	-	-	+	+	0.6	0.5	2 x 10^{-6}	32
16	+	+	-	-	10	3	1 x 10^{-7}	16

376

4.   Results and Discussion

4.1. CFD model validation

379 The developed CFD model was validated using the experimentally obtained data over a range of

380 feed inlet volumetric flow rates, $\dot{F}_f$ = 3.87, 7.94, 12.13, and 15.92 L/min. The permeate flux, J,

381 predictions from the CFD model were plotted against $\dot{F}_f$ in Fig. 4, along with their corresponding

382 experimental values. Since the CFD model results are very close to the experimental data, the CFD

383 predictions were deemed in good agreement with the experimental results. As shown in Fig. 4.,

20

384 higher feed flow rates result in enhanced water flux, due to the increase in the local heat transfer
385 coefficient at the feed side (h_f). The thermal boundary layer at the feed side becomes thinner with
386 increasing $\dot{F}_f$ and the temperature polarization effect diminishes [10,14,20].

387
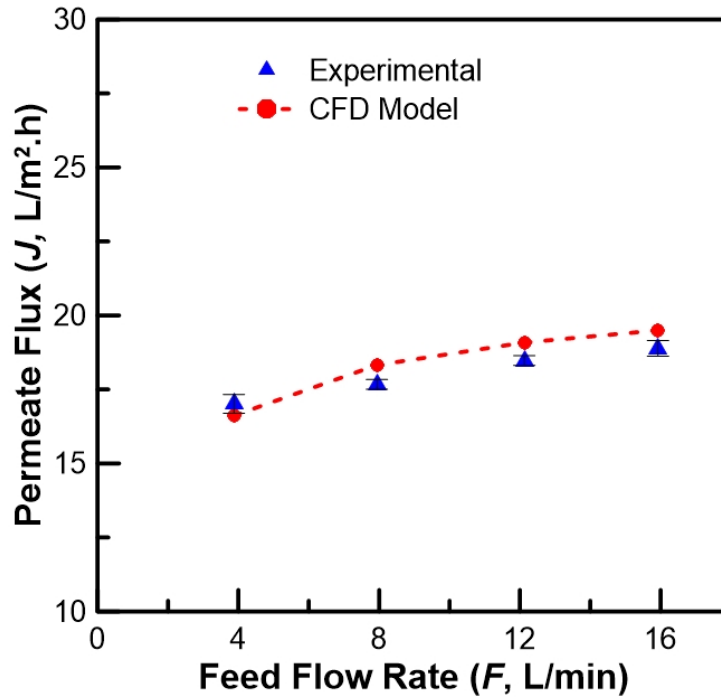
388
389

390 **Fig. 4.** CFD model validation using experimental permeate flux measurements over a range of
391 feed flow rates ($\dot{F}_f$ = 3.87, 7.94, 12.13 and 15.92 L/min).

392

393 The mentioned effect of feed flow rate on h_f was further examined using the CFD results. h_f was
394 monitored along the membrane length at the membrane/feed interface for four $\dot{F}_f$ values, as
395 presented in Fig. 5a. The shown h_f values were calculated at the centerline of the feed-side
396 boundary layer (Fig. 5b). Using a feed flow rate of 3.87 L/min as an example, the contour plot in
397 Fig. 5b shows the h_f profile at the membrane/feed interface. Additionally, the thermal boundary
398 layer on the feed side was monitored and contour plots were generated at the feed/membrane
399 interface for the four feed flow rates (Fig. 6). The boundary layer thickness was monitored using
400 the "wall distance" field function in Star-CCM+. The thermal boundary layer, shown in terms of
401 distance from the membrane surface in Fig. 6, was defined as any location where the temperature

402   is less than 99% of the bulk stream temperature. The contour plots in Fig. 6 clearly show that as

403   $\dot{F}_f$ increased, the thermal boundary layers became thinner, which supports the reasoning behind

404   the results in Fig. 5.

405
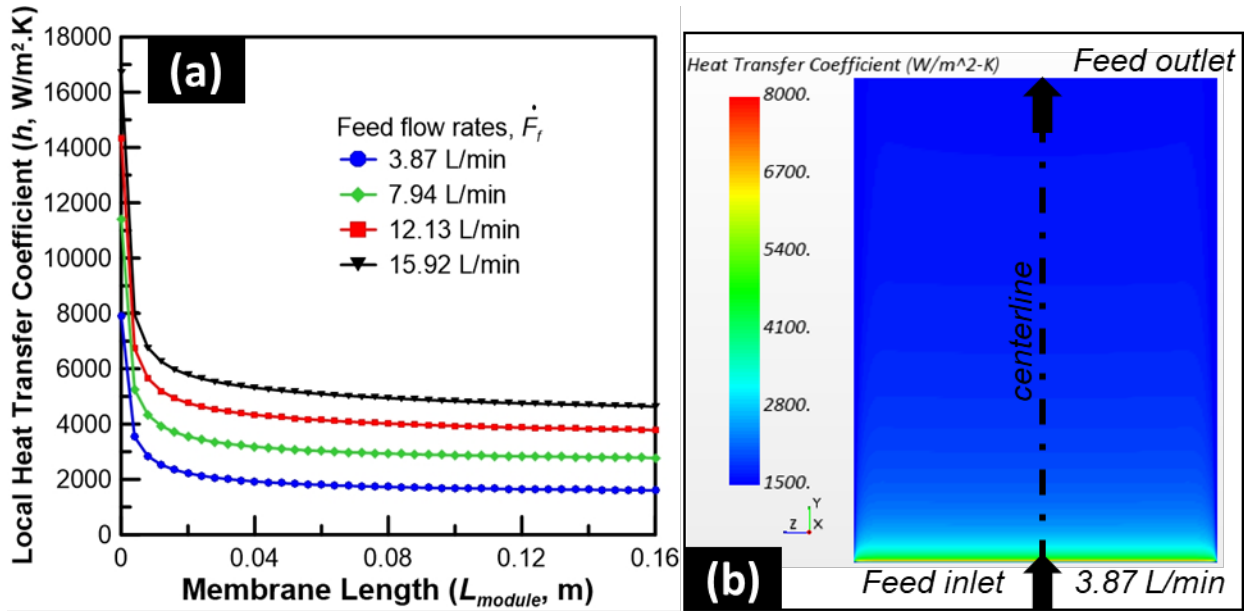
406

407   **Fig. 5.** (a) Local heat transfer coefficient (h) along the module length (L_{module}) at the centerline of
408   the feed channel boundary layer for varying feed inlet volumetric flow rates ($\dot{F}_f$ = 3.87, 7.94,
409   12.13 and 15.92 L/min). (b) Contour plot which shows the distribution of h along the feed side
410   boundary layer near the membrane/feed interface ($\dot{F}_f$ = 3.87 L/min).

411

412
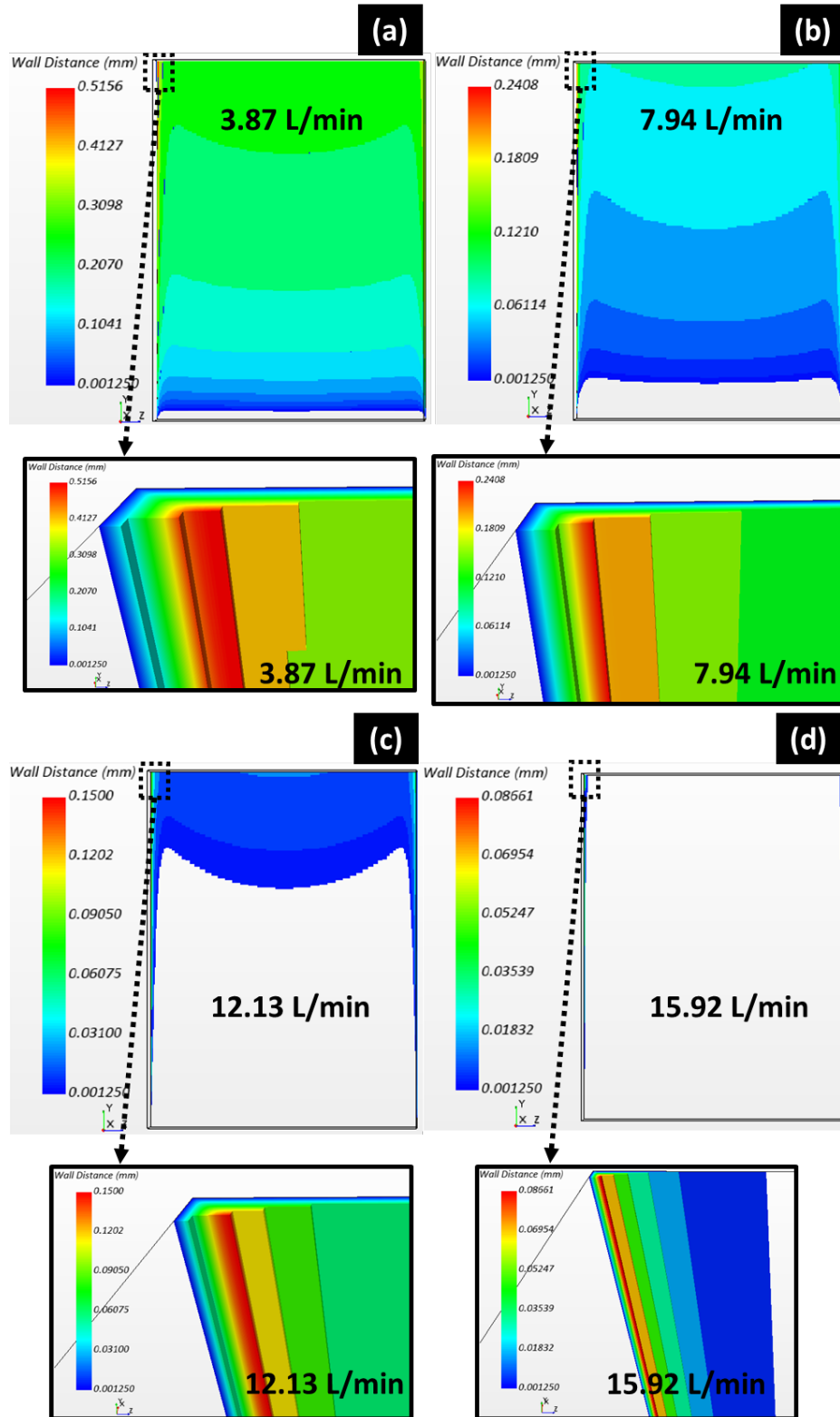
Fig. 6. Wall distance contour plots showing the change in thermal boundary layer thickness upon varying the feed flow rates: (a) $\dot{F}_f$ = 3.87 L/min (b) $\dot{F}_f$ = 7.94 L/min (c) $\dot{F}_f$ = 12.13 L/min and (d) $\dot{F}_f$ = 15.92 L/min.

4.2. Effects of system factors on J and η

After its validation, the CFD model was used to investigate the effects of the four system factors on J and η, based on the two-level full factorial design (table 3). The J and η values obtained from the CFD simulations are listed in Table 4. Different trends can be observed from the simulation results, which are in agreement with the literature-reported trade-offs between J and η for different MD configurations [42,43]. Run 7 yielded the highest J value, while the highest value for η was observed in Runs 11 and 12. Increasing L_{module} resulted in only a slight reduction of flux, which can be expected given the fact that even the longest module modeled (32 cm) is still relatively short (in comparison to full-scale MD systems), with tangible impacts of L_{module} hard to observe. Similarly, increasing L_{module} did not influence η, for the same reason as J. It merits mentioning that at significantly longer modules, both J and η are very likely to be affected in various ways, as we demonstrated in a previous study for DCMD and AGMD systems [40]. However, as a result of the fine grid used in our CFD modeling, which was needed to capture boundary layer effects, modeling much longer modules (e.g., on the order of meters) would have required a massive computational power unavailable to us.

Table 4. Design matrix table for responses (J and η) from the CFD model simulations at the two levels of four input factors (k_{gap}, δ_{gap}, B_m, and L_{module}). $\dot{F}_f$ was assumed 3.87 L/min (constant)

Run	k_{gap} [W/m K]	δ_{gap} [mm]	B_m [kg/m^2 s Pa]	L_{module} [cm]	J [L/m^2 h]	η [-]
1	10	3	2×10^{-6}	32	28.03	0.873
2	0.6	0.5	2×10^{-6}	16	24.31	0.889
3	10	0.5	2×10^{-6}	32	30.79	0.862
4	0.6	0.5	1×10^{-7}	16	4.19	0.262
5	10	0.5	1×10^{-7}	16	4.53	0.236
6	0.6	3	1×10^{-7}	16	2.68	0.326
7	10	0.5	2×10^{-6}	16	33.43	0.863
8	0.6	3	1×10^{-7}	32	2.61	0.325
9	10	3	1×10^{-7}	32	4.22	0.246
10	0.6	0.5	1×10^{-7}	32	4.02	0.261
11	0.6	3	2×10^{-6}	16	9.60	0.916
12	0.6	3	2×10^{-6}	32	9.34	0.915
13	10	0.5	1×10^{-7}	32	4.33	0.235
14	10	3	2×10^{-6}	16	30.25	0.874
15	0.6	0.5	2×10^{-6}	32	22.80	0.888
16	10	3	1×10^{-7}	16	4.40	0.247

Effects of factors on flux

The Pareto chart in Fig. 7 represents the significance level of the individual and interconnected factors on J in the dimensionless statistical form. The dimensionless statistical form aligns the ranking based on the standard deviations at a set confidence level (95% was used in our analysis). The t-value limit shown was calculated based on the identified significant parameters using half-normal plot, a tool which utilizes the ordered estimated effects in order to find the important factors under the 95% of significance threshold condition, using the Design-Expert software [25,41,44]. The blue columns indicate factors that are inversely proportional to the process output (J), while the orange columns indicate a direct proportionality. The factors/factor interactions are ranked from 1 to 15 based on the significance level. The bars below the t-value limit (rank 8 to rank 15) represent factors/ interactions which do not have any significant effects on J.
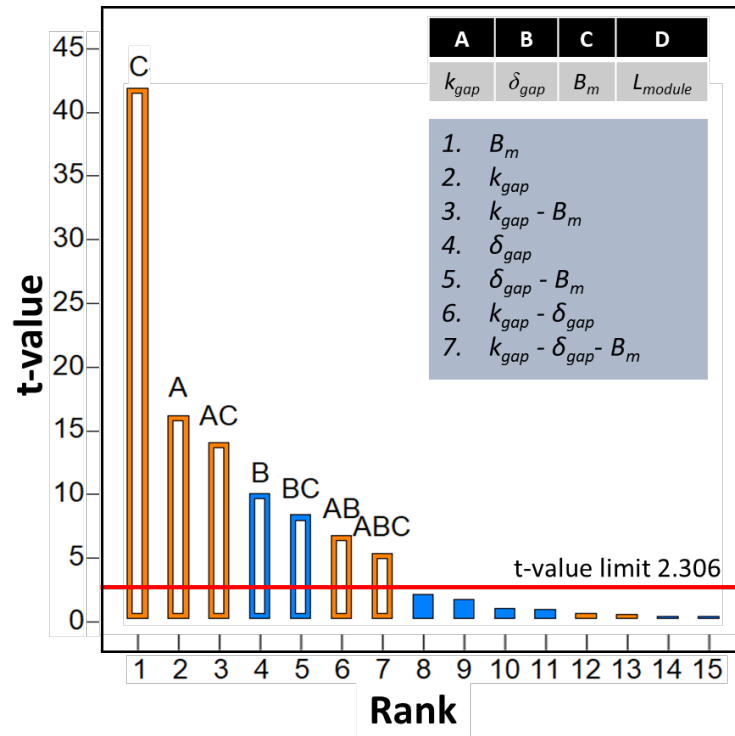
Fig. 7. Pareto chart of the effects of factors/factor interactions on J where the t-value of the absolute effects is plotted against the ranking. Rank 1 has the highest significance and 7 has the lowest significance. The bars below the t-value limit represent factors/ interactions which do not have any significant effects on J. The blue columns indicate factors that are inversely proportional to the process output (J), while the orange columns indicate a direct proportionality.

25

452

453   Based on the results shown in Fig. 7, J was found directly proportional to B_m, as expected from Eq.

454   1, with B_m having the most significant effect on J. Since a high gap conductance (k_{gap}/δ_{gap}) is

455   necessary for better process performance [6,7], k_{gap} and δ_{gap} were the following factors in terms of

456   impact, although the interaction of $k_{gap} - B_m$ was more important than δ_{gap}. The influence of L_{module}

457   was not as significant as those of other factors and interactions, as mentioned earlier.

458   Two types of interaction plots are given in Fig. 8 to further understand the above-mentioned trends.

459   In the 3D contour plots in Fig. 8, the x-axis and z-axis (horizontal axes) present the two factors of

460   interest, while the y-axis (vertical axis) shows the J values from the CFD model runs. The

461   remaining two factors (other than the two on the horizontal axes) were maintained at average

462   values when plotting the graphs. In the 2D interaction plots, J was plotted against one factor on

463   the x-axis. The two lines in each 2D interaction plot represent the upper- and lower-bounds of one

464   additional factor (the second factor of interest). Similar to the 3D contour plots, the remaining two

465   factors (other than those shown in the 2D interaction graph), were maintained at average values.

466   Interesting observations can be made from the graphs. The A–C plots illustrate the interaction

467   between k_{gap} and B_m. Even though the effect of k_{gap} on flux was significant for membranes with

468   high B_m (20 x 10^{-7} kg/m^2 Pa s), it had almost no effect on flux for the membrane with low B_m (1 x

469   10^{-7} kg/m^2 Pa s). A similar observation can be made for δ_{gap} from the B–C plots. δ_{gap} was inversely

470   proportional to J at high B_m (20 x 10^{-7} kg/m^2 Pa s) and an increase in δ_{gap} from 0.5 mm to 3 mm

471   enhanced the flux as expected [8]. But, at low B_m (1 x 10^{-7} kg/m^2 Pa s), this effect was very minute.

472   On the other hand, the $k_{gap} - \delta_{gap}$ interaction (on the A–B plots) showed that the effect of k_{gap} on J

473   was more evident at the higher δ_{gap} value (3 mm).

474   The flux is driven by the overall temperature difference between the hot and cold streams. The

475   resistance of the hot stream, membrane, gap, condensation plate and the cold stream are in series.

476   Since these resistances are in series, the total resistance between the hot and cold channels can be

477   evaluated as the sum of all the resistances (extending Eq. 14 across all the resistance terms). Within

478   the membrane, the resistances to vapor transport and to conduction can be considered to be in

479   parallel, since they represent two alternative pathways for heat transfer through the membrane.

480   If one of these 5 resistances is significantly larger than the rest, the sum is dominated by this

481   resistance. In such a scenario, changing this resistance would have a significant impact on overall

482 heat transfer, whereas modifying the others would have minimal impact. In light of this discussion,

483 we can understand the trends observed in Fig. 8. At low B_m, the membrane is the major resistance

484 in the series. In this scenario, therefore, changing k_{gap} has a small influence on flux. In contrast, at

485 high B_m, the gap itself is the major resistance. Therefore, increasing k_{gap} in this case leads to

486 significant improvement in flux. The observed trends of the impact of δ_{gap} at the different values

487 of B_m can also be explained by the same logic.

488 Similarly, at large δ_{gap}, the gap resistance is larger. In such a scenario, changes to the gap resistance

489 by changing k_{gap} are more significant, rather than when δ_{gap} is small and the gap resistance itself

490 is correspondingly small.

491
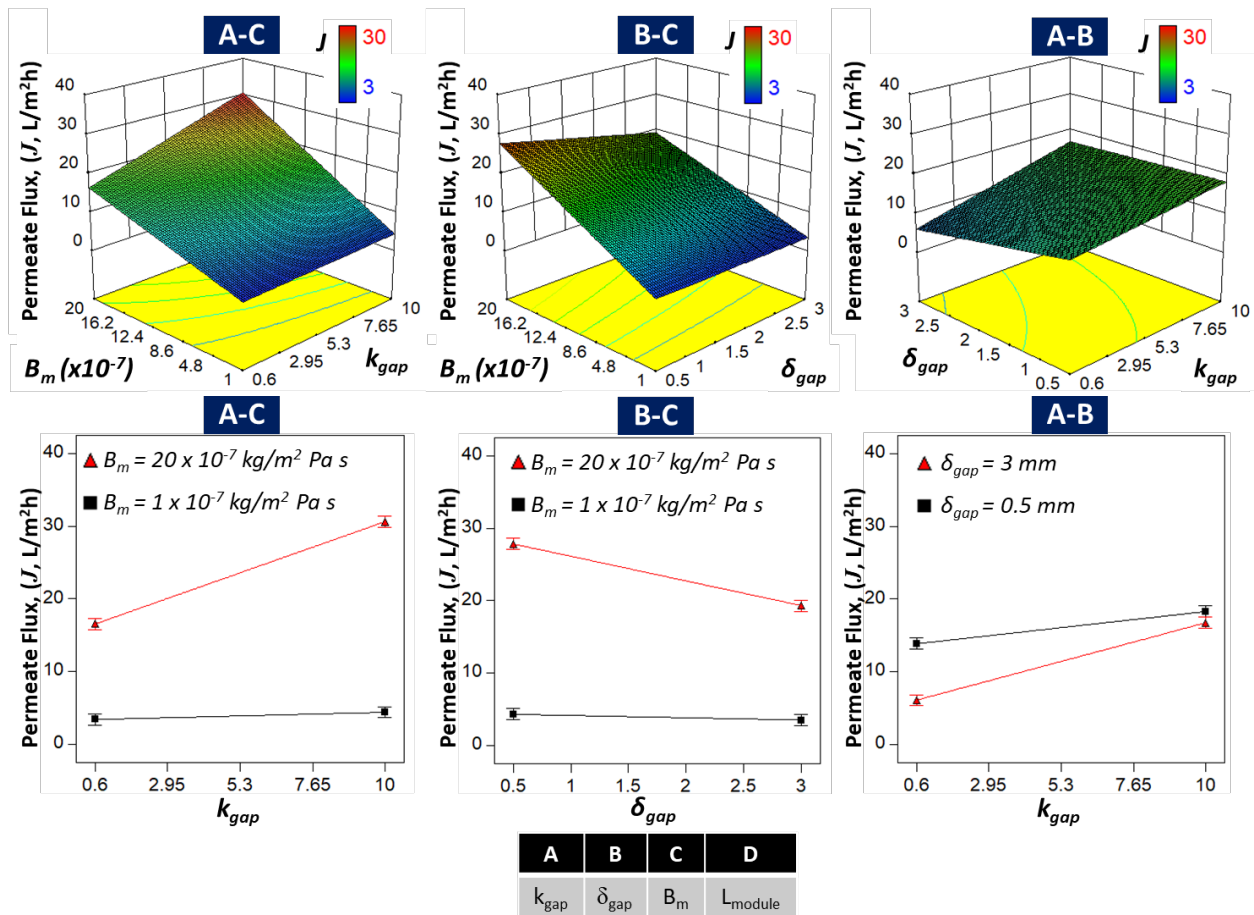
Fig. 8. 3D contour and 2D interaction graphs for the permeate flux (J) response, where A–C is the $k_{gap} - B_m$ interaction, B–C is the $\delta_{gap} - B_m$ interaction, and A–B is the $k_{gap} - \delta_{gap}$ interaction. The error bars in the 2D graphs indicate the 95% least significant difference interval for the data points.

496

Effects of factors on thermal efficiency

The Pareto chart in Fig. 9 displays the impact ranking of the different factors/factor interactions on η based on the CFD simulations results in Table 4. The blue columns indicate factors that are inversely proportional to the process output (η), while the orange columns indicate direct proportionality. The factors/factor interactions are ranked from 1 to 15 based on the significance level. The bars below the t-value limit (rank 1 to rank 4) indicate factors/interactions without any significant effects on η. The results show that B_m, k_{gap}, and δ_{gap} all have effects on η, with B_m having, by far, the most significant effect. The significance levels of k_{gap} and δ_{gap} followed, in that order. The only significant factor interaction vis-à-vis η was the $k_{gap} - \delta_{gap}$ interaction, which came fourth in the rank of significance. This factor interaction is presented in the 2D interaction and 3D contour graphs in Fig. 9. Based on the heat transfer mechanism in PGMD, an increase in gap conductance (k_{gap}/δ_{gap}) is necessary to achieve better process performance [6,7]. Therefore, the significance of the $k_{gap} - \delta_{gap}$ interaction was observed as expected.

Going back to the heat transfer resistance model of the MD process, η defines the fraction of the total energy transfer happening in the form of vapor flux through the membrane. Not surprisingly therefore, the permeability has a significant impact on η. An increase in B_m improves vapor transport through the membrane without affecting the heat conduction resistance, thereby significantly improving η.
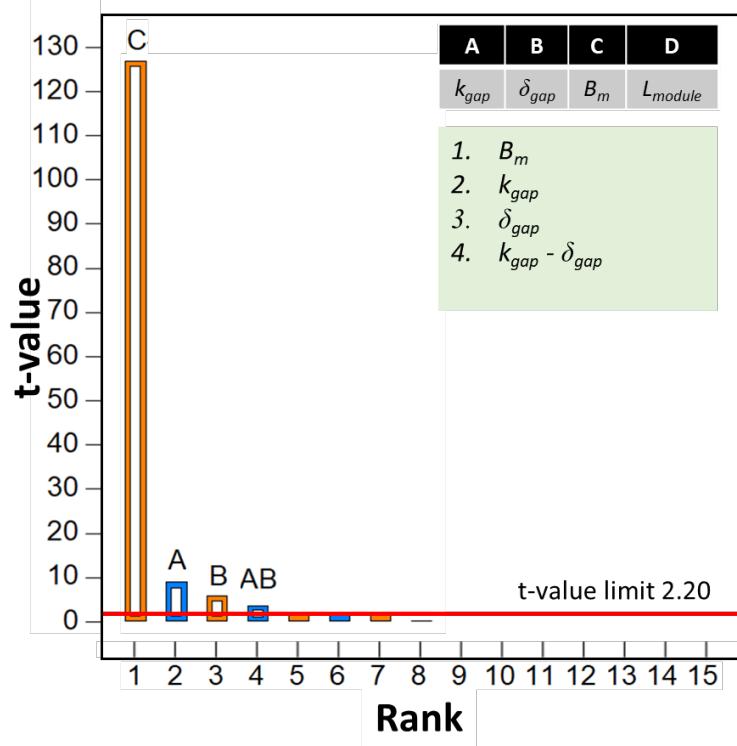
Fig. 9. Pareto chart of the effects of factors/factor interactions on η where the t-value of the absolute effects is plotted against the ranking. Rank 1 has the highest significance and 4 has the lowest significance. The bars below the t-value limit represent factors/interactions which do not have any significant effects on η. The blue columns indicate factors that are inversely proportional to the process output (η), while the orange columns indicate direct proportionality.
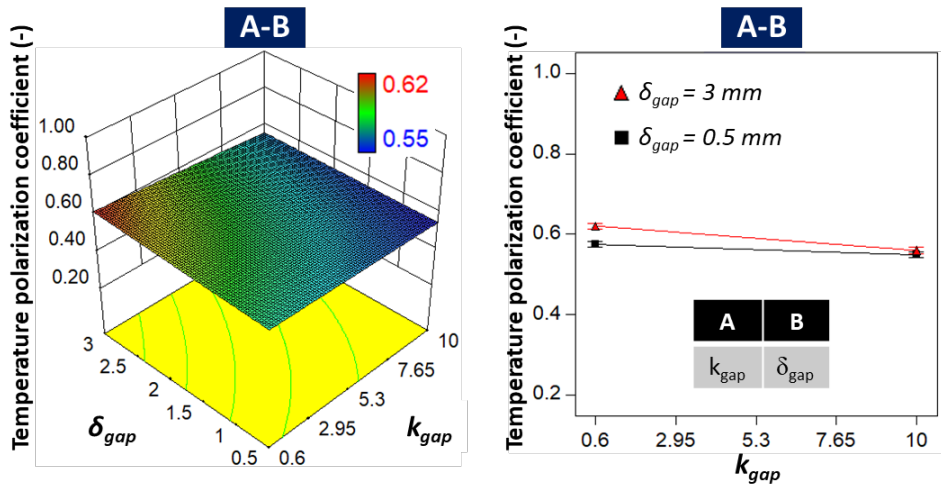
Fig. 10. 3D contour and 2D interaction graphs for the η process output obtained from CFD model runs. A–B is the $k_{gap} - \delta_{gap}$ interaction.

29

5. Conclusion

In this study, a CFD model was developed for the PGMD configuration and was validated using experimental data. Upon validation of the model, a factorial analysis statistical tool was used to design the simulation sets to evaluate the influence of four selected PGMD configuration parameters (k_{gap}, δ_{gap}, L_{module} and B_m) on flux, J, and thermal efficiency, η. The latter two were selected as key indicators of process performance. The model reveals the influence of module design parameters in maximizing both J and η. The results show that B_m, k_{gap}, and δ_{gap} each have a significant contribution to PGMD process performance. Additionally, factorial analysis was a useful tool to probe the significance of each factor by also considering the interactions among parameters.

In view of the analysis, the following conclusions were reached:

- The membrane distillation coefficient has the most substantial effect on J and η in PGMD. This term has a positive correlation with both J and η.
- The next largest effects are from k_{gap} (positive correlation with J) and δ_{gap} (negative correlation with J), individually, although the effect the $k_{gap} - B_m$ interaction is more significant than δ_{gap} with respect to its impact on J.
- The $k_{gap} - B_m$ (positive correlation with J), $\delta_{gap} - B_m$ (negative correlation with J), and $k_{gap} - \delta_{gap}$ (positive correlation with J) interactions all have significant impacts on J, in the order listed.
- The effect of k_{gap} on J is more significant for membranes with high B_m, because the gap resistance becomes the dominant resistance at high B_m.
- The only significant factor interaction observed for η was that of $k_{gap} - \delta_{gap}$. This interaction has a negative correlation with η.

Acknowledgment

References

[1]   N. Thomas, M.O. Mavukkandy, S. Loutatidou, H.A. Arafat, Membrane distillation research & implementation: Lessons from the past five decades, Sep. Purif. Technol. 189 (2017) 108–127. doi:10.1016/j.seppur.2017.07.069.

[2]   L. Eykens, I. Hitsov, K. De Sitter, C. Dotremont, L. Pinoy, I. Nopens, B. Van der Bruggen, Influence of membrane thickness and process conditions on direct contact membrane distillation at different salinities, J. Memb. Sci. 498 (2016) 353–364. doi:10.1016/j.memsci.2015.07.037.

[3]   E. Drioli, A. Ali, F. Macedonio, Membrane distillation: Recent developments and perspectives, Desalination. 356 (2015) 56–84. doi:10.1016/j.desal.2014.10.028.

[4]   J. Swaminathan, H.W. Chung, D.M. Warsinger, F.A. AlMarzooqi, H.A. Arafat, J.H. Lienhard, Energy efficiency of permeate gap and novel conductive gap membrane distillation, J. Memb. Sci. 502 (2016) 171–178. doi:10.1016/j.memsci.2015.12.017.

[5]   L. Cheng, Y. Zhao, P. Li, W. Li, F. Wang, Comparative study of air gap and permeate gap membrane distillation using internal heat recovery hollow fiber membrane module, Desalination. 426 (2018) 42–49. doi:10.1016/j.desal.2017.10.039.

[6]   J. Swaminathan, H.W. Chung, D.M. Warsinger, J.H. Lienhard V, Membrane distillation model based on heat exchanger theory and configuration comparison, Appl. Energy. 184 (2016) 491–505. doi:10.1016/j.apenergy.2016.09.090.

[7]   J. Swaminathan, H.W. Chung, D.M. Warsinger, J.H. Lienhard V, Energy efficiency of membrane distillation up to high salinity: Evaluating critical system size and optimal membrane thickness, Appl. Energy. 211 (2018) 715–734. doi:10.1016/j.apenergy.2017.11.043.

[8]   L. Eykens, T. Reyns, K. De Sitter, C. Dotremont, L. Pinoy, B. Van der Bruggen, How to select a membrane distillation configuration? Process conditions and membrane influence unraveled, Desalination. 399 (2016) 105–115. doi:10.1016/j.desal.2016.08.019.

[9]   R.G. Raluy, R. Schwantes, V.J. Subiela, B. Peñate, G. Melián, J.R. Betancort, Operational experience of a solar membrane distillation demonstration plant in Pozo Izquierdo-Gran

582   Canaria Island (Spain), Desalination. 290 (2012) 1–13. doi:10.1016/j.desal.2012.01.003.

583   [10]   L. Francis, N. Ghaffour, A.A. Alsaadi, G.L. Amy, Material gap membrane distillation: A
584   new design for water vapor flux enhancement, J. Memb. Sci. 448 (2013) 240–247.
585   doi:10.1016/j.memsci.2013.08.013.

586   [11]   J. Swaminathan, Unified Framework to Design Efficient Membrane Distillation for Brine
587   Concentration, (2017) 1–219.

588   [12]   H. Cho, Y.-J. Choi, S. Lee, J. Koo, T. Huang, Comparison of hollow fiber membranes in
589   direct contact and air gap membrane distillation (MD), Desalin. Water Treat. (2015) 1–8.
590   doi:10.1080/19443994.2015.1038113.

591   [13]   D. Winter, J. Koschikowski, M. Wieghaus, Desalination using membrane distillation:
592   Experimental studies on full scale spiral wound modules, J. Memb. Sci. 375 (2011) 104–
593   112. doi:10.1016/j.memsci.2011.03.030.

594   [14]   A. Cipollina, M.G. Di Sparti, A. Tamburini, G. Micale, Development of a Membrane
595   Distillation module for solar energy seawater desalination, Chem. Eng. Res. Des. 90 (2012)
596   2101–2121. doi:10.1016/j.cherd.2012.05.021.

597   [15]   D. Winter, Membrane distillation – a thermodynamic, technological and economic analysis
598   Ph.D. thesis, 2014.

599   [16]   A. Deshmukh, C. Boo, V. Karanikola, S. Lin, A.P. Straub, T. Tong, D.M. Warsinger, M.
600   Elimelech, Membrane distillation at the water-energy nexus: Limits, opportunities, and
601   challenges, Energy Environ. Sci. 11 (2018) 1177–1196. doi:10.1039/c8ee00291f.

602   [17]   A. Deshmukh, M. Elimelech, Understanding the impact of membrane properties and
603   transport phenomena on the energetic performance of membrane distillation desalination,
604   J. Memb. Sci. 539 (2017) 458–474. doi:10.1016/j.memsci.2017.05.017.

605   [18]   F. Mahmoudi, G. Moazami Goodarzi, S. Dehghani, A. Akbarzadeh, Experimental and
606   theoretical study of a lab scale permeate gap membrane distillation setup for desalination,
607   Desalination. 419 (2017) 197–210. doi:10.1016/j.desal.2017.06.013.

608   [19]   A. Hagedorn, G. Fieg, D. Winter, J. Koschikowski, T. Mann, Methodical design and
609   operation of membrane distillation plants for desalination, Chem. Eng. Res. Des. 125 (2017)

610   265–281. doi:10.1016/j.cherd.2017.07.024.

[20]   A. Ruiz-Aguirre, J.A. Andrés-Mañas, J.M. Fernández-Sevilla, G. Zaragoza, Modeling and optimization of a commercial permeate gap spiral wound membrane distillation module for seawater desalination, Desalination. 419 (2017) 160–168. doi:10.1016/j.desal.2017.06.019.

[21]   H. Ahadi, J. Karimi-Sabet, M. Shariaty-Niassar, T. Matsuura, Experimental and numerical evaluation of membrane distillation module for oxygen-18 separation, (2018). doi:10.1016/j.cherd.2018.01.042.

[22]   I. Hitsov, T. Maere, K. De Sitter, C. Dotremont, I. Nopens, Modelling approaches in membrane distillation: A critical review, Sep. Purif. Technol. 142 (2015) 48–64. doi:10.1016/j.seppur.2014.12.026.

[23]   M.M.A. Shirazi, A. Kargari, A.F. Ismail, T. Matsuura, Computational Fluid Dynamic (CFD) opportunities applied to the membrane distillation process: State-of-the-art and perspectives, Desalination. 377 (2016) 73–90. doi:10.1016/j.desal.2015.09.010.

[24]   R.W. Mee, A Comprehensive Guide to Factorial Two-Level Experimentation, Springer, 2009.

[25]   J. Antony, Design of Experiments for Engineers and Scientists, Second edi, Elsevier, 2014. doi:10.1016/B978-0-08-099417-8.

[26]   M. Essalhi, M. Khayet, Fundamentals of membrane distillation, Elsevier Ltd, 2015. doi:10.1016/B978-1-78242-246-4.00010-6.

[27]   E. Karbasi, J. Karimi-Sabet, J. Mohammadi-Rovshandeh, M. Ali Moosavian, H. Ahadi, Y. Amini, Experimental and numerical study of air-gap membrane distillation (AGMD): Novel AGMD module for Oxygen-18 stable isotope enrichment, Chem. Eng. J. 322 (2017) 667–678. doi:10.1016/j.cej.2017.03.031.

[28]   A.N. Mabrouk, , Yasser Elhenawy, M. Abdelkader, M. Shatat, The impact of baffle orientation on the performance of the hollow fiber membrane, Desalin. Water Treat. 58 (2017) 35–45. doi:10.5004/dwt.2017.0030.

[29]   L. Zhang, J. Xiang, P.G. Cheng, N. Tang, H. Han, L. Yuan, H. Zhang, S. Wang, X. Wang, Three-dimensional numerical simulation of aqueous NaCl solution in vacuum membrane

638   distillation process, Chem. Eng. Process. Process Intensif. 87 (2015) 9–15.
639   doi:10.1016/j.cep.2014.11.002.

640 [30] X. Yang, H. Yu, R. Wang, A.G. Fane, Analysis of the effect of turbulence promoters in
641   hollow fiber membrane distillation modules by computational fluid dynamic (CFD)
642   simulations, J. Memb. Sci. 415–416 (2012) 758–769. doi:10.1016/j.memsci.2012.05.067.

643 [31] X. Yang, H. Yu, R. Wang, A.G. Fane, Optimization of microstructured hollow fiber design
644   for membrane distillation applications using CFD modeling, J. Memb. Sci. 421–422 (2012)
645   258–270. doi:10.1016/j.memsci.2012.07.022.

646 [32] N. Tang, H. Zhang, W. Wang, Computational fluid dynamics numerical simulation of
647   vacuum membrane distillation for aqueous NaCl solution, Desalination. 274 (2011) 120–
648   129. doi:10.1016/j.desal.2011.01.078.

649 [33] Siemens Product Lifecycle Management Software Inc, Star-CCM+, (2018).

650 [34] V.Y. Agbodemegbe, X. Cheng, E.H.K. Akaho, F.K.A. Allotey, Correlation for cross-flow
651   resistance coefficient using STAR-CCM+ simulation data for flow of water through rod
652   bundle supported by spacer grid with split-type mixing vane, Nucl. Eng. Des. 285 (2015)
653   134–149. doi:10.1016/j.nucengdes.2015.01.003.

654 [35] V.Y. Agbodemegbe, X. Cheng, E.H.K. Akaho, F.K.A. Allotey, An investigation of the
655   effect of split-type mixing vane on extent of crossflow between subchannels through the
656   fuel rod gaps, Ann. Nucl. Energy. 88 (2016) 174–185. doi:10.1016/j.anucene.2015.10.036.

657 [36] B. Lian, Y. Wang, P. Le-Clech, V. Chen, G. Leslie, A numerical approach to module design
658   for crossflow vacuum membrane distillation systems, J. Memb. Sci. 510 (2016) 489–496.
659   doi:10.1016/j.memsci.2016.03.041.

660 [37] J.B. Swaminathan, Numerical and Experimental Investigation of Membrane Distillation
661   Flux and Energy Efficiency, (2014).

662 [38] C.Y. Iguchi, W.N. dos Santos, R. Gregorio, Determination of thermal properties of
663   pyroelectric polymers, copolymers and blends by the laser flash technique, Polym. Test. 26
664   (2007) 788–792. doi:10.1016/j.polymertesting.2007.04.009.

665 [39] H. Yu, X. Yang, R. Wang, A.G. Fane, Numerical simulation of heat and mass transfer in

666   direct membrane distillation in a hollow fiber module with laminar flow, J. Memb. Sci. 384
667   (2011) 107–116. doi:10.1016/j.memsci.2011.09.011.

668   [40]   M.I. Ali, E.K. Summers, H.A. Arafat, J.H. Lienhard V, Effects of membrane properties on
669   water production cost in small scale membrane distillation systems, Desalination. 306
670   (2012) 60–71. doi:10.1016/j.desal.2012.07.043.

671   [41]   Stat-Ease Inc., Design-Expert® Version 10, (2018).

672   [42]   X. Yang, R. Wang, A.G. Fane, Novel designs for improving the performance of hollow
673   fiber membrane distillation modules, J. Memb. Sci. 384 (2011) 52–62.
674   doi:10.1016/j.memsci.2011.09.007.

675   [43]   Q. He, P. Li, H. Geng, C. Zhang, J. Wang, H. Chang, Modeling and optimization of air gap
676   membrane distillation system for desalination, Desalination. 354 (2014) 68–75.
677   doi:10.1016/j.desal.2014.09.022.

678   [44]   M. Shah, K. Pathak, Development and Statistical Optimization of Solid Lipid Nanoparticles
679   of Simvastatin by Using 23 Full-Factorial Design, AAPS PharmSciTech. 11 (2010) 489–
680   496. doi:10.1208/s12249-010-9414-z.